














RESEARCH ARTICLE | OCTOBER 12 2023

Mid-infrared photocurrent nano-spectroscopy exploiting the thermoelectric effect in graphene

T. Venanzi ; V. Giliberti ; M. E. Temperini ; S. Sotgiu ; R. Polito ; F. Mattioli ; A. Pitanti ; V. Mišeikis ; C. Coletti ; S. Roddaro ; L. Baldassarre ; M. Ortolani  

 Check for updates

Appl. Phys. Lett. 123, 153509 (2023)

<https://doi.org/10.1063/5.0162631>



View Online



Export Citation



Applied Physics Letters

Special Topic:

Quantum Networks

Guest Editors: David Awschalom, Ronald Hanson, Stephanie Simmons

Submit Today!

Mid-infrared photocurrent nano-spectroscopy exploiting the thermoelectric effect in graphene

Cite as: Appl. Phys. Lett. **123**, 153509 (2023); doi: [10.1063/5.0162631](https://doi.org/10.1063/5.0162631)

Submitted: 15 June 2023 · Accepted: 23 September 2023 ·

Published Online: 12 October 2023



View Online



Export Citation



CrossMark

T. Venanzi,¹  V. Giliberti,¹  M. E. Temperini,^{1,2}  S. Sotgiu,²  R. Polito,²  F. Mattioli,³  A. Pitanti,⁴ 
V. Mišeikis,^{5,6}  C. Coletti,^{5,6}  S. Roddaro,⁷  L. Baldassarre,²  and M. Ortolani^{2,a)} 

AFFILIATIONS

¹Center for Life Nano-Science, Istituto Italiano di Tecnologia, 00161 Rome, Italy

²Department of Physics, Sapienza University of Rome, 00185 Rome, Italy

³CNR-Istituto di Fotonica e Nanotecnologie, 00156 Rome, Italy

⁴NEST, CNR-Istituto Nanoscienze and Scuola Normale Superiore, 56127 Pisa, Italy

⁵Graphene Labs, Istituto Italiano di Tecnologia, 16163 Genoa, Italy

⁶Center for Nanotechnology Innovation @NEST, Istituto Italiano di Tecnologia, 56126 Pisa, Italy

⁷Department of Physics, University of Pisa, 56127 Pisa, Italy

^{a)} Author to whom correspondence should be addressed: michele.ortolani@roma1.infn.it

ABSTRACT

We develop a conductive-atomic force microscope coupled to a mid-infrared (IR) quantum cascade laser that allows to measure mid-IR photocurrent maps and spectra with nanometric spatial resolution. Here, we exploit the photo-induced thermoelectric effect of graphene to obtain the mid-IR local absorption spectra of nanoscale devices and materials. By scanning the probe in AFM-contact mode, the thermoelectric photocurrent can be mapped throughout the graphene layer, which acts as a semitransparent transducer. At zero voltage bias applied to the probe tip, we observe very low noise (about 25 pA/ $\sqrt{\text{Hz}}$), which makes our technique competitive with others in measuring the local IR absorption in nanomaterials with insufficient thermal expansion coefficient, or to characterize nanoscale devices that significantly absorb IR radiation, such as mid-infrared photodetectors.

© 2023 Author(s). All article content, except where otherwise noted, is licensed under a Creative Commons Attribution (CC BY) license (<http://creativecommons.org/licenses/by/4.0/>). <https://doi.org/10.1063/5.0162631>

Mid-infrared (MIR) spectroscopy at the nanoscale has become an accessible experimental tool with the development of scanning probe techniques. Light beams are focused onto nanometric probes, and in this way, the diffraction limit for MIR spectroscopic imaging has been overcome. Detection can be optical, as in scattering-scanning near-field optical microscopy (s-SNOM),^{1,2} mechanical, as in photo-induced force microscopy (PiFM)^{3,4} and in atomic-force microscopy-IR (AFM-IR),⁵ which are based on the atomic force microscopy signal modulation by an IR beam, or electrical, as in photocurrent microscopy,^{6–9} where the probe only acts as the local light source scanned through the sample area. A different class of techniques that also makes use of light beams coupled to AFM probes to study the photo-response of materials at the nanoscale¹⁰ is photoconductive atomic force microscopy (PC-AFM). In this case, the AFM probe is conductive and it is used as one electrode to contact the sample for measuring the effect of light on the electron transport. So far, PC-AFM setups have worked in the visible/near infrared (VIS/NIR) only, mostly to investigate the nanoscale inhomogeneities of photovoltaic devices.^{10–12}

Despite the great interest in MIR integrated devices, PC-AFM has yet to be employed in the MIR. In this wavelength range, photothermal effects typically become dominant over electron-hole pair generation and different challenges must be tackled to perform MIR PC-AFM measurements with controlled lateral resolution and with low electrical noise.

In this work, we present the development of a conductive-AFM (C-AFM) setup coupled to a MIR tunable quantum cascade laser (QCL) capable to measure a photocurrent in nanoscale conductive devices. We acquire both photocurrent spectra by sweeping the laser wavelength at specific AFM-probe positions on the sample, and photocurrent maps at fixed MIR wavelength with a lateral resolution of about 50 nm, i.e., about $\lambda/100$. In our experiment, the conductive AFM probe is put in contact with a graphene layer that, being semitransparent, allows the IR light to reach the material under test below the graphene layer. We observe photocurrent at zero voltage bias compatible with the thermoelectric effect due to the transient photo-induced temperature gradients that form in the sample portion below

the probe tip. This zero-bias PC-AFM mode is extremely useful for measuring the photothermal properties of inorganic devices with insufficient thermal expansion coefficient that prevents the use of the more mature AFM-IR technique. In general, our technique could be used to characterize any MIR photodetector or any sub-micron device that significantly absorbs MIR radiation.

The atomic force microscope is a commercial AFM-IR setup (*NanoIR2* by Bruker-Anasys) that operates in contact-mode and is coupled to a mid-infrared QCL (*MIRcat-xB* by Daylight Solutions). The QCL is tunable between 5 and 12 μm wavelength (900–1900 cm^{-1} wavenumber). The laser beam is focused on the probe tip with a parabolic mirror (angle of incidence of 70° and focal length of 75 mm) and the position of the focus is finely controlled with computer-controlled plane mirrors. Radiation field enhancement at the conductive tip apex heats the nanometric region below the tip much more than the rest of the diffraction-limited spot size (plasmonic hot-spot effect). In the AFM-IR mode, the MIR absorption spectrum of the sample is measured mechanically by monitoring the amplitude of the cantilever oscillation,⁵ while in this work, it is the photocurrent that is measured with similar spectroscopic aim. We use solid-platinum *Rocky Mountain* probes to ensure a stable electrical and mechanical contact, with tip radius of about 20 nm.

We customized the *NanoIR2* by electrically contacting the AFM probe and the sample and by adding an external electric measurement circuit composed of a multimeter, a lock-in amplifier (SR860 by Stanford Research Systems), and a low-noise transimpedance amplifier (by Femto) as depicted in the sketch in Fig. 1(a), effectively replicating a C-AFM setup. A low-pass filter prevents sudden electrostatic discharges (ESD) through the conductive tip. Figures 1(b) and 1(c) show two examples of C-AFM measurements on MoS_2 and graphene. The semiconducting MoS_2 flake is exfoliated on a gold substrate that is used as counter electrode. We observe a diode-like dependence of the

current on the applied voltage in agreement with C-AFM measurements reported in the literature.¹³ Differently, the graphene stripe deposited on SiO_2/Si displays an Ohmic behavior (4.6 $\text{k}\Omega$) with a series resistance, which is the sum of intrinsic graphene, metal contact, scanning probe, and tip/graphene junction resistances.

For the PC-AFM measurements, we modulate the QCL beam with a mechanical chopper at 227 Hz. The chopper frequency is set to be much lower than the QCL repetition rate (about 100 kHz) to avoid recording signals due to laser heating or radiation pressure on the cantilever. The customized setup allows for simultaneous acquisition of the AFM topography, the AFM-IR photothermal expansion, and the MIR photocurrent, enabling to correlate all these signals under the same experimental conditions and with the probe tip located on the sample with the nanometric precision typical of AFMs.

Figure 2(a) shows a sketch of the illuminated AFM probe scanning on a metal-contacted graphene stripe deposited on a $\text{SiO}_2(285\text{ nm})/\text{Si}$ substrate. Monolayer graphene is grown via chemical vapor deposition (CVD) on Cu foil¹⁴ and is deposited on top of the substrate with Au electrodes using semi-dry transfer.¹⁵ More details on sample fabrication are given in the supplementary material. Figure 2(b) shows the photocurrent at three different MIR incident powers at $\lambda = 6.26\ \mu\text{m}$ ($\omega = 1600\ \text{cm}^{-1}$). We observe a nonzero current at zero bias and a negative slope of the MIR photo-induced I–V characteristics [photocurrent direction opposite to DC direction, see Fig. 1(c) for reference]. As extensively discussed in the literature,^{16–19} the total infrared photocurrent in graphene is given by the sum of the photothermoelectric effect (PTE), the photo-voltaic effect, and the bolometric effect. The photoresponse under zero bias observed in Fig. 2(b) is due to the PTE, i.e., the Seebeck effect in both graphene stripe and Pt tip portions where temperature gradients exist. With a voltage bias applied, the photo-voltaic and bolometric responses of graphene kick in and contribute to the total photocurrent.¹⁶ One can discern between the three effects by tuning the Fermi energy of the graphene, but this goes beyond the scope of this work. In addition to these infrared absorption mechanism in graphene, there is the thermoelectric effect (TE) of graphene due to IR absorption in the material on which graphene is laid on: being graphene semi-transparent, if that material displays a nonzero absorption coefficient, its temperature will increase and the graphene temperature will correspondingly increase, thereby inducing a thermoelectric response in graphene.¹⁷ As expected in all mentioned effects, the infrared photoresponse shows a linear dependence on the incident MIR power (see the supplementary material).

A photocurrent spectrum under zero tip-electrode bias of graphene is shown in Fig. 2(c). The most evident feature is the sharp phonon peak of SiO_2 centered at about $1100\ \text{cm}^{-1}$. At this laser frequency, the infrared photocurrent of the device is dominated by the absorption of the SiO_2 substrate phonons that transfer heat to the graphene layer.¹⁷ At other wavenumbers, where the SiO_2 absorption coefficient is nearly zero, an infrared photoresponse is still observed and must be due to the broadband absorption of graphene and it is due partly to interband and partly to intraband absorption with proportions depending on the Fermi level.²⁰ Free electron losses in the platinum tip may also play a role in MIR absorption. Figure 2(c) shows the AFM-IR photoexpansion spectrum (top blue curve) measured from the AC-coupled AFM channel simultaneously to the PC-AFM spectrum (red curves). For this choice of sample and AFM probe, the PC-AFM spectrum taken at zero voltage bias is less noisy than the AFM-IR

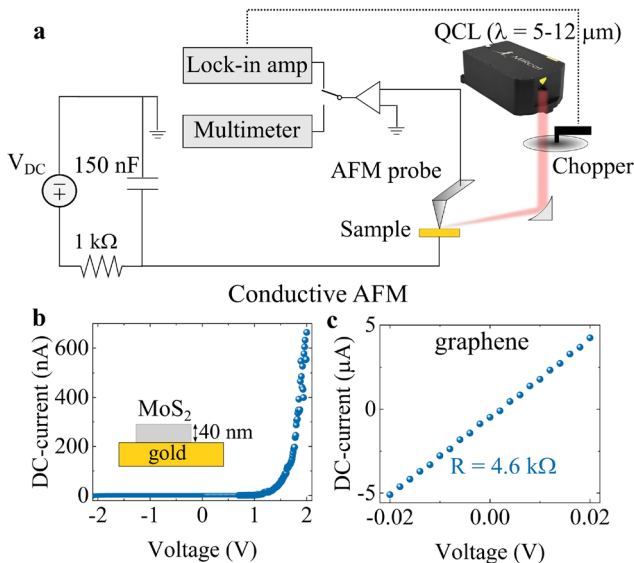


FIG. 1. (a) Sketch of the electrical circuit and the AFM-IR setup. (b) and (c) Conductive-AFM IV-sweep of a MoS_2 40-nm-thick flake placed on a gold substrate and of a CVD-grown graphene monolayer.

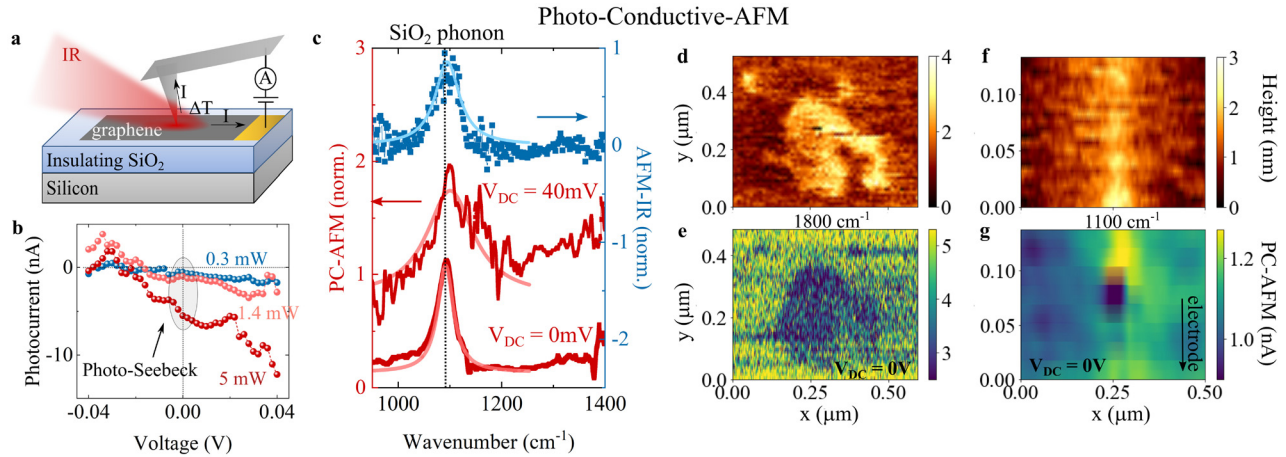


FIG. 2. (a) Sketch of the experiment geometry. (b) Photocurrent at $\lambda = 6.25 \mu\text{m}$ at different incident peak power and voltages. (c) Spectra of PC-AFM (red) and AFM-IR (blue) of graphene on SiO_2/Si substrate. The PC-AFM and the AFM-IR spectra are measured simultaneously. The fitting function is a Lorentzian function. The PC-AFM spectra are measured under zero bias and 40 mV bias. (d) and (e) AFM topography and PC-AFM map at 1800 cm^{-1} wavenumber of an adsorbate on the surface of graphene, respectively. (f) and (g) AFM topography and PC-AFM map at 1100 cm^{-1} wavenumber of a graphene wrinkle.

spectrum. The signal-to-noise ratio (SNR) of PC-AFM at finite voltage bias [Fig. 2(c), $V_{\text{DC}} = 40 \text{ mV}$] between tip and substrate is not as good since it is dominated by the mechanical noise figure related to the intermittent contact of the AFM probe to the sample that impacts on the direction and intensity of the local DC electric field. At zero bias, the intermittent AFM contact does not play any role (there is no local DC field and the resistance modulation is negligible if compared to other series resistances) and the noise is dominated by QCL intensity fluctuations, typically of the order of 0.1% RMS. At zero bias, we observe $25 \text{ pA}/\sqrt{\text{Hz}}$ (SNR of about 200 in 1 s integration time per spectral point with a signal of 5 nA and a peak laser input power of 100 mW at 1100 cm^{-1} and 2.5% duty cycle).

To describe the mapping capabilities of MIR PC-AFM, we show two examples where its nanometric spatial resolution plays a crucial role in the identification of surface topography features. Figures 2(d) and 2(e) show the AFM topography and a PC-AFM map at 1800 cm^{-1} of adsorbates on the graphene surface, where the absolute value of the photocurrent has been used. In the presence of adsorbates on the surface, the tip-to-sample electrical contact degrades and we observe a strong decrease in the PC-AFM signal. Surface sensitivity is maximized by choosing a MIR wavenumber (here, 1800 cm^{-1}) at which the substrate is almost transparent and PTE in graphene is the dominant phenomenon. As a second example, Fig. 2(f) shows the AFM topography of a wrinkle, which has a lateral size of about 30 nm, length of several micrometers, and a height of about 2 nm. Wrinkles are typical in CVD-grown graphene and can originate either at the growth stage or at the substrate transfer stage. The MIR PC-AFM map at 1100 cm^{-1} across the wrinkle is shown in Fig. 2(g). Along the wrinkle, we observe a maximum and a minimum in the photocurrent [yellow and dark blue spots in Fig. 2(g)]. These features must correspond to charge puddles.^{21,22} Sensitivity to nanoscale thermal conductivity patterns is, therefore, maximized by choosing a MIR wavenumber (here, 1100 cm^{-1}) at which the substrate strongly absorbs the radiation.

The lateral resolution of the PC-AFM maps in Figs. 2(e) and 2(g) is about 50 nm, which is comparable to the resolution of the related AFM topography (see the supplementary material), and

therefore, the lateral resolution is about $\lambda/160$. We notice that, as in C-AFM or in VIS/NIR-PC-AFM,¹⁰ the definition of lateral resolution is given as the precision with which objects (or edges) are located starting from the sub-nanometric positioning precision of the probe. However, differently from C-AFM and similarly to AFM-IR, the lateral resolution for measuring absorption inhomogeneity in the case of homogeneous electrical contact is not limited by the diffraction limit but it is given by the plasmonic field-enhancement volume at the apex of the metallic tip and by the complicated interplay between thermal capacitance and conductivity of all materials and structures.^{23,24} A typical scale is $\sim 300 \text{ nm}$, still well below the diffraction limit.²⁵

We now discuss the physical origin of the observed photocurrent under zero bias, which is one of the key advantages of the MIR PC-AFM method. The graphene stripe and the platinum probe operate as a thermocouple that measures the heat generated by the MIR radiation. The sample absorbs MIR radiation mostly in the hotspot at the tip apex, which roughly corresponds to the thermocouple junction. The heat generated by MIR absorption produces temperature gradients along the tip shaft and the graphene stripe. Through the Seebeck effect, two electromotive forces will be generated in the stripe and in the tip, but a net photo-induced voltage is observed due to the different Seebeck coefficients of graphene S_{graphene} (tens of $\mu\text{V}/\text{K}$ at the expected doping of our sample^{14,26,27}) and platinum S_{tip} ($-5 \mu\text{V}/\text{K}$ ²⁸). This thermoelectric voltage is ultimately proportional to the temperature difference ΔT between the junction and the reservoir (the sample at equilibrium T_0 under pulsed MIR illumination). The monolayer graphene stripe is almost transparent to MIR radiation; therefore, the highest T may be rather reached in the sample material that more strongly absorbs the radiation, such as SiO_2 , which however does not participate to the thermoelectric effect. Depending on the sample thermal conductance and capacitance, the temperature increase may last longer than the laser pulse length (about 200 ns), and therefore, the measured quasi-DC voltage ΔV (chopper frequency of 227 Hz) is being built up for a longer time, eventually approaching the inverse repetition rate $f_{\text{QCL}} = 120 \text{ kHz}$:

$$\Delta V = f_{QCL} \int_0^{\frac{1}{f_{QCL}}} \Delta T(t) (S_{\text{graphene}} - S_{\text{tip}}) dt. \quad (1)$$

The voltage signal could be optimized in the future by increasing ($S_{\text{graphene}} - S_{\text{tip}}$). To this aim, field-effect gate bias of the graphene stripe and/or probes made of different materials, such as boron-doped diamond, can be used. In perspective, a thermocouple could be integrated in the probe tip itself so as to make the technique independent of the presence of the graphene stripe on the sample.^{29,30}

Finally, we employ the thermoelectric effect of graphene to perform infrared spectroscopy on thin flakes of a 2D material. We present results of hBN since the literature of MIR nano-spectroscopy is very rich and well-documented³¹ and other 2D semiconductors, such as MoS₂, do not have phonon resonances in the MIR range. We deposit thin hBN layers on a gold substrate by mechanical exfoliation and then we stamp on top of them the graphene flakes via deterministic transfer³² [sketch in Fig. 3(a)]. The graphene is in electrical contact with the gold substrate which is used as bottom electrode. Figure 3(b) shows an AFM map of the graphene/hBN heterostructure on the gold substrate. Figures 3(c) and 3(d) show the comparison of PC-AFM (red curves) and AFM-IR (blue curves) spectra taken on two hBN flakes with different thicknesses (more details in the supplementary material). Both spectra show a narrow absorption peak that corresponds to the transverse optical (TO) phonon. Moreover, the thick hBN/graphene heterostructure shows a broad absorption band at about 1300 cm⁻¹. This band is likely due to a low-quality factor open cavity with an Au backplane as reported in the literature, e.g., in Ref. 33, excited in our experiment with 70° angle of incidence.

Nano-spectroscopy performed by AFM-IR and PC-AFM carries essentially the same physical information related to local absorption, even though it is obtained by measuring different derived quantities. A fair comparison of SNR obtained with the two techniques on the same sample can be done by looking at Fig. 3(c), where AFM-probes optimized for each technique have

been employed, at odds with Fig. 2(c): a gold-coated silicon probe for AFM-IR, and a solid-platinum probe for PC-AFM. The two techniques perform similarly in terms of SNR on hBN, with PC-AFM performed at zero bias. The PC-AFM can be advantageous with respect to AFM-IR for sample with low thermal expansion and gives further degrees of freedom such as the possibility to change the transducer material and to apply a voltage which is necessary to measure photoconductive devices.

In conclusion, we have performed photocurrent measurements with nanometric scanning probes and laser illumination in the mid-infrared. We have exploited the thermoelectric effect in graphene to measure the infrared absorption spectra of a thin SiO₂ layer and of a 20-nm-thick hBN flakes demonstrating the capability of PC-AFM to perform nano-IR spectroscopy. Maps with 50 nm spatial resolution, which is two orders of magnitude smaller than the employed IR wavelength, have been acquired to characterize nanometric-size inhomogeneities such as wrinkles and IR-absorbing adsorbates in graphene. A key feature of the PC-AFM technique is that the electrical detection can be performed at zero bias, which, depending on sample properties, may give a SNR advantage over both photoexpansion techniques that rely on relatively noisy mechanical detection, and electrical detection techniques that cannot be performed at zero bias.

See the supplementary material for further experimental details regarding the sample fabrication process and characterization, the lateral resolution of PC-AFM, and the origin of the hBN peak observed in Fig. 3.

We acknowledge financial support from PNRR MUR Project No. PE000023-NQSTI and from the European Union's Horizon 2020 Research and Innovation Program under Grant Agreement No. 881603-Graphene Core3.

AUTHOR DECLARATIONS

Conflict of Interest

The authors have no conflicts to disclose.

Author Contributions

Tommaso Venanzi: Conceptualization (equal); Investigation (lead); Methodology (equal); Software (equal); Writing – original draft (equal); Writing – review & editing (supporting). **Stefano Roddaro:** Investigation (supporting); Resources (supporting); Writing – review & editing (supporting). **Leonetta Baldassarre:** Funding acquisition (equal); Methodology (supporting); Writing – review & editing (supporting). **Michele Ortolani:** Conceptualization (equal); Funding acquisition (equal); Investigation (supporting); Methodology (equal); Resources (lead); Supervision (equal); Writing – original draft (equal); Writing – review & editing (lead). **Valeria Gilberti:** Conceptualization (equal); Investigation (supporting); Methodology (equal); Writing – review & editing (supporting). **Maria Eleonora Temperini:** Investigation (supporting); Methodology (supporting); Software (equal). **Simone Sotgiu:** Investigation (supporting). **Raffaella Polito:** Investigation (supporting); Methodology (supporting). **Francesco Mattioli:** Investigation (supporting). **Alessandro Pitanti:** Investigation (supporting). **Vaidotas Mišeikis:** Investigation (supporting). **Camilla Coletti:** Resources (supporting).

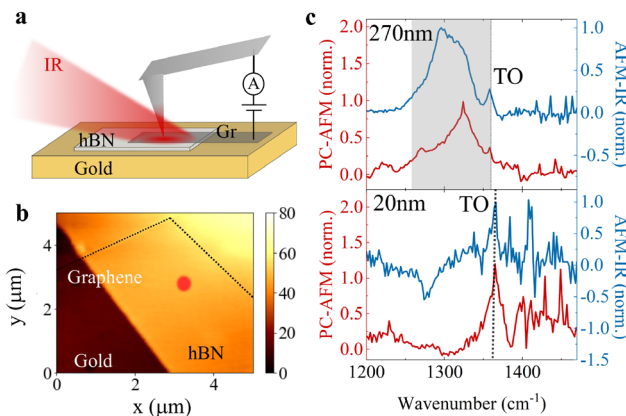


FIG. 3. (a) Sketch of the PC-AFM spectroscopy experiment of hBN flakes. (b) AFM topography of the hBN/graphene heterostructure on gold. (c) PC-AFM (red) and AFM-IR (blue) spectra of hBN/graphene. The graphene is indicated by the dashed line in Fig. 3(b). The upper panel shows the spectra of a 270-nm-thick hBN flake that shows both the hBN TO phonon mode and a broad feature that we interpret as a low-quality open cavity mode with an Au backplane. The lower panel shows a spectrum of thin hBN flake that features a single phonon peak.

DATA AVAILABILITY

The data that support the findings of this study are available from the corresponding author upon reasonable request.

REFERENCES

- ¹B. Knoll and F. Keilmann, "Near-field probing of vibrational absorption for chemical microscopy," *Nature* **399**, 134–137 (1999).
- ²X. Chen, D. Hu, R. Mescall, G. You, D. Basov, Q. Dai, and M. Liu, "Modern scattering-type scanning near-field optical microscopy for advanced material research," *Adv. Mater.* **31**, 1804774 (2019).
- ³A. Ambrosio, M. Tamagnone, K. Chaudhary, L. A. Jauregui, P. Kim, W. L. Wilson, and F. Capasso, "Selective excitation and imaging of ultraslow phonon polaritons in thin hexagonal boron nitride crystals," *Light* **7**, 1 (2018).
- ⁴D. Nowak, W. Morrison, H. K. Wickramasinghe, J. Jahng, E. Potma, L. Wan, R. Ruiz, T. R. Albrecht, K. Schmidt, J. Frommer *et al.*, "Nanoscale chemical imaging by photoinduced force microscopy," *Sci. Adv.* **2**, e1501571 (2016).
- ⁵J. Mathurin, A. Deniset-Besseau, D. Bazin, E. Dartois, M. Wagner, and A. Dazzi, "Photothermal AFM-IR spectroscopy and imaging: Status, challenges, and trends," *J. Appl. Phys.* **131**, 010901 (2022).
- ⁶A. Woessner, P. Alonso-González, M. B. Lundeberg, Y. Gao, J. E. Barrios-Vargas, G. Navickaite, Q. Ma, D. Janner, K. Watanabe, A. W. Cummings *et al.*, "Near-field photocurrent nanoscopy on bare and encapsulated graphene," *Nat. Commun.* **7**, 10783 (2016).
- ⁷S. S. Sunku, D. Halbertal, T. Stauber, S. Chen, A. S. McLeod, A. Rikhter, M. E. Berkowitz, C. F. B. Lo, D. E. Gonzalez-Acevedo, J. C. Hone *et al.*, "Hyperbolic enhancement of photocurrent patterns in minimally twisted bilayer graphene," *Nat. Commun.* **12**, 1641 (2021).
- ⁸E. A. Pogna, M. Asgari, V. Zannier, L. Sorba, L. Viti, and M. S. Vitiello, "Unveiling the detection dynamics of semiconductor nanowire photodetectors by terahertz near-field nanoscopy," *Light* **9**, 189 (2020).
- ⁹N. Rauhut, M. Engel, M. Steiner, R. Krupke, P. Avouris, and A. Hartschuh, "Antenna-enhanced photocurrent microscopy on single-walled carbon nanotubes at 30 nm resolution," *ACS Nano* **6**, 6416–6421 (2012).
- ¹⁰D. C. Coffey, O. G. Reid, D. B. Rodovsky, G. P. Bartholomew, and D. S. Ginger, "Mapping local photocurrents in polymer/fullerene solar cells with photoconductive atomic force microscopy," *Nano Lett.* **7**, 738–744 (2007).
- ¹¹L. S. Pingree, O. G. Reid, and D. S. Ginger, "Imaging the evolution of nanoscale photocurrent collection and transport networks during annealing of polythiophene/fullerene solar cells," *Nano Lett.* **9**, 2946–2952 (2009).
- ¹²J. Choi, H. Zhang, and J. H. Choi, "Modulating optoelectronic properties of two-dimensional transition metal dichalcogenide semiconductors by photoinduced charge transfer," *ACS Nano* **10**, 1671–1680 (2016).
- ¹³F. Giannazzo, G. Fisichella, A. Piazza, S. Agnello, and F. Roccaforte, "Nanoscale inhomogeneity of the Schottky barrier and resistivity in MOS₂ multilayers," *Phys. Rev. B* **92**, 081307 (2015).
- ¹⁴V. Miseikis, F. Bianco, J. David, M. Gemmi, V. Pellegrini, M. Romagnoli, and C. Coletti, "Deterministic patterned growth of high-mobility large-crystal graphene: A path towards wafer scale integration," *2D Mater.* **4**, 021004 (2017).
- ¹⁵M. A. Giambra, V. Miseikis, S. Pezzini, S. Marconi, A. Montanaro, F. Fabbri, V. Sorianello, A. C. Ferrari, C. Coletti, and M. Romagnoli, "Wafer-scale integration of graphene-based photonic devices," *ACS Nano* **15**, 3171–3187 (2021).
- ¹⁶M. Freitag, T. Low, F. Xia, and P. Avouris, "Photoconductivity of biased graphene," *Nat. Photonics* **7**, 53–59 (2013).
- ¹⁷M. Badioli, A. Woessner, K.-J. Tielrooij, S. Nanot, G. Navickaite, T. Stauber, F. J. Garcia de Abajo, and F. H. Koppens, "Phonon-mediated mid-infrared photo-response of graphene," *Nano Lett.* **14**, 6374–6381 (2014).
- ¹⁸L. Vicarelli, M. Vitiello, D. Coquillat, A. Lombardo, A. C. Ferrari, W. Knap, M. Polini, V. Pellegrini, and A. Tredicucci, "Graphene field-effect transistors as room-temperature terahertz detectors," *Nat. Mater.* **11**, 865–871 (2012).
- ¹⁹Y. Yao, R. Shankar, P. Rauter, Y. Song, J. Kong, M. Loncar, and F. Capasso, "High-responsivity mid-infrared graphene detectors with antenna-enhanced photocurrent generation and collection," *Nano Lett.* **14**, 3749–3754 (2014).
- ²⁰K. F. Mak, L. Ju, F. Wang, and T. F. Heinz, "Optical spectroscopy of graphene: From the far infrared to the ultraviolet," *Solid State Commun.* **152**, 1341–1349 (2012).
- ²¹S. Samaddar, I. Yudhistira, S. Adam, H. Courtois, and C. Winkelmann, "Charge puddles in graphene near the Dirac point," *Phys. Rev. Lett.* **116**, 126804 (2016).
- ²²J. C. Koepke, J. D. Wood, D. Estrada, Z.-Y. Ong, K. T. He, E. Pop, and J. W. Lyding, "Atomic-scale evidence for potential barriers and strong carrier scattering at graphene grain boundaries: A scanning tunneling microscopy study," *ACS Nano* **7**, 75–86 (2013).
- ²³J. J. Schwartz, G. Pavlidis, and A. Centrone, "Understanding cantilever transduction efficiency and spatial resolution in nanoscale infrared microscopy," *Anal. Chem.* **94**, 13126–13135 (2022).
- ²⁴A. Mancini, V. Giliberti, A. Alabastri, E. Calandrini, F. De Angelis, D. Garoli, and M. Ortolani, "Thermoplasmonic effect of surface-enhanced infrared absorption in vertical nanoantenna arrays," *J. Phys. Chem. C* **122**, 13072–13081 (2018).
- ²⁵M. B. Lundeberg, Y. Gao, A. Woessner, C. Tan, P. Alonso-González, K. Watanabe, T. Taniguchi, J. Hone, R. Hillenbrand, and F. H. Koppens, "Thermoelectric detection and imaging of propagating graphene plasmons," *Nat. Mater.* **16**, 204–207 (2017).
- ²⁶X. Cai, A. B. Sushkov, R. J. Suess, M. M. Jadidi, G. S. Jenkins, L. O. Nyakiti, R. L. Myers-Ward, S. Li, J. Yan, D. K. Gaskill *et al.*, "Sensitive room-temperature terahertz detection via the photothermoelectric effect in graphene," *Nat. Nanotechnol.* **9**, 814–819 (2014).
- ²⁷A. Harzheim, C. Evangeli, O. V. Kolosov, and P. Gehring, "Direct mapping of local Seebeck coefficient in 2D material nanostructures via scanning thermal gate microscopy," *2D Mater.* **7**, 041004 (2020).
- ²⁸M. Kockert, R. Mitdank, A. Zykov, S. Kowarik, and S. Fischer, "Absolute Seebeck coefficient of thin platinum films," *J. Appl. Phys.* **126**, 105106 (2019).
- ²⁹A. Hammiche, H. Pollock, M. Reading, M. Claybourn, P. Turner, and K. Jewkes, "Photothermal FT-IR spectroscopy: A step towards FT-IR microscopy at a resolution better than the diffraction limit," *Appl. Spectroscopy* **53**, 810–815 (1999).
- ³⁰A. M. Katzenmeyer, G. Holland, J. Chae, A. Band, K. Kjoller, and A. Centrone, "Mid-infrared spectroscopy beyond the diffraction limit via direct measurement of the photothermal effect," *Nanoscale* **7**, 17637–17641 (2015).
- ³¹J. D. Caldwell, I. Aharonovich, G. Cassabois, J. H. Edgar, B. Gil, and D. Basov, "Photonics with hexagonal boron nitride," *Nat. Rev. Mater.* **4**, 552–567 (2019).
- ³²A. Castellanos-Gomez, M. Buscema, R. Molenaar, V. Singh, L. Janssen, H. S. Van Der Zant, and G. A. Steele, "Deterministic transfer of two-dimensional materials by all-dry viscoelastic stamping," *2D Mater.* **1**, 011002 (2014).
- ³³M. Barra-Burillo, U. Muniain, S. Catalano, M. Autore, F. Casanova, L. E. Hueso, J. Aizpurua, R. Esteban, and R. Hillenbrand, "Microcavity phonon polaritons from the weak to the ultrastrong phonon-photon coupling regime," *Nat. Commun.* **12**, 6206 (2021).